

Controlling factors of superconductivity and emergence of magnetism in $A_x(\text{NH}_3)_y\text{Fe}_{2-\delta}(\text{Se}_{1-z}\text{Te}_z)_2$ ($A = \text{Li}$ and Na)

Hechang Lei,^{1,†} Jiangang Guo,^{1,†} Fumitaka Hayashi,² and Hideo Hosono,^{1,2,3,*}

¹ Materials Research Center for Element Strategy, Tokyo Institute of Technology, Yokohama 226-8503, Japan

² Frontier Research Center, Tokyo Institute of Technology, Yokohama 226-8503, Japan

³ Materials and Structures Laboratory, Tokyo Institute of Technology, Yokohama 226-8503, Japan

Abstract

The discovery of superconductivity in alkali-ammonia co-intercalated FeSe has generated intensive interest because of their highest T_c (~ 45 K) among iron-chalcogenide superconductors with bulk form. On the other hand, for most iron-based superconductors, superconductivity is located near an antiferromagnetic state, suggesting the importance of magnetic interaction for superconductivity. Therefore, it is important to establish whether these intercalated compounds also obey this correlation. Here, we report the phase diagrams of two series of $\text{Li}_x(\text{NH}_3)_y\text{Fe}_2(\text{Se}_{1-z}\text{Te}_z)_2$ and $\text{Na}_x(\text{NH}_3)_y\text{Fe}_2(\text{Se}_{1-z}\text{Te}_z)_2$. Superconductivity is suppressed by Te doping gradually, accompanied by the emergence of magnetic ordering states. Moreover, a novel phase $\text{Li}_x(\text{NH}_3)_y\text{Fe}_{2-\delta}\text{Te}_2$ with possible antiferromagnetism is discovered. This strongly indicates the intimate relation between superconductivity and magnetism in these materials. Comparative structure analysis with $\text{FeSe}_{1-z}\text{Te}_z$ suggests there are more controlling factors in superconductivity for iron-chalcogenide superconductors compared with iron-pnictide superconductors, possibly related to the different chemical features of the two families. It opens up an opportunity to tune the superconductivity in iron-chalcogenide superconductors in more ways than just one.

Introduction

The superconductivity of FePn-based superconductors (SCs) is usually in the vicinity of magnetic ordering states (1-3), leading to a possible unconventional superconducting mechanism and intricate interplay (competition and/or coexistence) between superconductivity and magnetism (4,5). Similarly, the superconducting states in FeCh-based (Ch = S, Se, and Te) SCs are also near the magnetic ordering states (6-10), such as the emerging spin glass (SG) state in $K_xFe_{2-y}(Se, S)_2$ with S doping (8), the antiferromagnetism (AFM) with $(\pi, 0)$ in-plane magnetic wave vector in FeTe (9) and the recently discovered antiferromagnetic and semiconducting/insulating state in β -Fe $_{1-x}$ Se with particular Fe-vacancy orders (10).

On the other hand, after summarizing a large amount of experimental data, the superconducting transition temperature T_c of FePn-based SCs is closely related to two structural parameters, the bond angle (α and β) of Pn-Fe-Pn (Pn = P and As) and the anion height from the Fe layer (h) (11, 12). In general, T_c increases when α and β approach the angle of a regular tetrahedron (109.47°), or h is close to the optimal value (~ 1.38 Å). These correlations can partially explain the trends in T_c for some FeCh-based (Ch = S, Se, and Te) SCs, such as the enhancement of T_c in FeSe with pressure that could be related to the decrease of h to the optimal value (13, 14), and the decrease of T_c in $K_xFe_{2-y}(Se, S)_2$ that is ascribed to the increase of bond angles of Ch-Fe-Ch (8). However, these are many exceptions. For example, even though the anion height of intercalated FeSe is far from the optimal value, its T_c (~ 30 K) is still much larger than that of FeSe (15). The T_c of FeSe with better α/β and h is lower than that of FeTe $_{0.53}$ Se $_{0.47}$ (11, 12). Thus, the question of whether the T_c is influenced by the same factors in FePn- and FeCh-based SCs is still under debate.

Recently, superconductivity with T_c up to 45 K has been reported in $A_x(NH_3/NH_2)_yFe_2Se_2$ (A = alkali, alkali-earth and rare-earth metals) synthesized by the low-temperature ammonothermal method (16-19). Until now, it is still unknown whether this newly discovered superconducting family has a similar magnetic/superconducting phase diagram as in other iron-based SCs, which is vitally

important to understanding the relationship between superconductivity and magnetism in these materials. On the other hand, this system is a good platform to study the relationship between structure and superconductivity in FeCh-based SCs because the FeSe layer is almost intact (few Fe vacancy) even after intercalation. This avoids the complexities of structure and property found in high-temperature-synthesized $A_x\text{Fe}_{2-\delta}\text{Ch}_2$ ($A = \text{K}, \text{Rb}, \text{Cs}, \text{ and } \text{Tl}$) due to the formation of a large amount of Fe vacancies (20-22). Here, we systematically studied the phase diagrams of two series of $\text{Li}_x(\text{NH}_3)_y\text{Fe}_{2-\delta}(\text{Se}_{1-z}\text{Te}_z)_2$ and $\text{Na}_x(\text{NH}_3)_y\text{Fe}_{2-\delta}(\text{Se}_{1-z}\text{Te}_z)_2$ ($0 \leq z \leq 1$) (abbreviated as Li/NaNH₃-122). The detailed magnetic characterization indicates that the superconducting states in these compounds are close to the magnetic ordering states. Moreover, the comparative structure analysis with $\text{FeSe}_{1-z}\text{Te}_z$ indicates that there are more factors that influence T_c in FeCh-based SCs than in FePn-based SCs.

Results and Discussion

Figure 1a and b show the c - and a -axial lattice parameters of Li/NaNH₃-122 as determined from the powder X-ray diffraction (PXRD) (Supplementary Fig. 1) using the structure of $\text{Li}_{0.6}(\text{ND}_{2.8})\text{Fe}_2\text{Se}_2$ (Fig. 1c) as an initial model (17). The fitted lattice parameters of $\text{FeSe}_{1-z}\text{Te}_z$ from PXRD patterns (Supplementary Fig. 2) are also plotted for comparison. The a - and c -axial lattice parameters for both Li/NaNH₃-122 and $\text{FeSe}_{1-z}\text{Te}_z$ increase almost linearly with Te doping, confirming the substitution of Se by larger Te. It should be noted that the coexistence of two phases in $\text{FeSe}_{1-z}\text{Te}_z$ with $0.1 \leq z \leq 0.5$ (Supplementary Fig. 2) leads to similar behaviors in the intercalated compounds (Fig. 1a and b), which are different from samples synthesized using a high-temperature method where all of the starting materials are fused together (22). In the two-phase region, one phase (Phase 1) has smaller a - and c -axial lattice parameters than the other one (Phase 2), possibly because of the lower Te content in Phase 1 than in Phase 2. Although the c -axial lattice parameters of Li/NaNH₃-122 are remarkably larger than those of $\text{FeSe}_{1-z}\text{Te}_z$ due to the co-intercalation with NH_3 and NH_2^- (Fig. 1a), the relative increase $[(d_{(00l), z=0} - d_{(00l), z=0.9})/d_{(00l), z=0}]$ of Li/NaNH₃-122 ($\sim 11.6\%$ and 7.8% , respectively) is smaller than that in $\text{FeSe}_{1-z}\text{Te}_z$ ($\sim 13.6\%$). It can

be ascribed to the less change of thick Li-/Na-NH₃(NH₂⁻) layers with Te doping that weakens the influence of the change of Fe(Se, Te) layer on the *c*-axial lattice parameters. The fact that the *a*-axial lattice parameters of Li/NaNH₃-122 are slightly larger than those of FeSe_{1-z}Te_z at certain *z* values indicates that the Fe(Se, Te) layers are stretched after intercalation (Fig. 1b). The relative change of the *a*-axial lattice parameters is ~ 1.8 % and 1.9 % for LiNH₃-122 and NaNH₃-122, respectively, close to the value of ~ 1.4 % in FeSe_{1-z}Te_z but much smaller than those values for the *c* axis. It suggests that the interlayer interaction between the Fe(Se, Te) layers is much weaker than intralayer one. Interestingly, for FeTe, Li can be intercalated and the PXRD pattern fits well using the isostructure of Li_{0.6}(ND_{2.8})Fe₂Se₂ (Fig. 1d). In contrast, Na cannot be intercalated into FeTe completely (Supplementary Fig. 3), unlike the situation in the counterpart FeSe. This could be due to the smaller ionic size of Li⁺ than Na⁺ and the different chemical features of FeTe and FeSe.

The chemical composition analyses of Li/NaNH₃-122 (Supplementary Table 1) show that the actual molar ratios of Se to Te are comparable to those in FeSe_{1-z}Te_z (Supplementary Table 2). On the other hand, there is no systematic change of Na content with Te doping, which fluctuates between ~ 0.45 and 0.8. These values are close to the previous results for (Li/Na/K)_x(NH₃)_yFe_{2-δ}Se₂ (17-19). Ion chromatography (IC) analysis indicates that the NH₃ (*y*) content for the whole series ranges between ~ 0.3 and 0.8, close to the results reported in the literature (17, 18), assuming that all nitrogen species originate from NH₃ molecules. Most strikingly, the Fe vacancies (~ 1 - 10 %, Supplementary Table 1) are much lower than those of high-temperature-synthesized A_xFe_{2-δ}Ch₂ (~ 10 - 25 %) (20, 21), which has significant effects on the magnetism of samples at the normal state discussed below.

As shown in Figure 2a and b, the onset of *T_c* is 41.4 K and 45.7 K for (Li/Na)_x(NH₃)_yFe_{2-δ}Se₂, respectively, consistent with the reported results (16, 17). With increasing Te content, the *T_c* shift to the lower temperature and there are two transitions for 0.2 ≤ *z* ≤ 0.4, due to the coexistence of two phases. When doping Te further (*z* ≥ 0.5), the two transitions converge again, with even lower *T_c*s. Finally, the superconducting transition cannot be observed above 2 K for both LiNH₃-122 and

NaNH₃-122 with $z \geq 0.8$. Except for the sample with $z = 0.7$, all of the superconducting samples exhibit large superconducting volume fractions (SVFs), clearly indicating bulk superconductivity. In order to confirm that the absence of superconductivity in the samples with $z \geq 0.8$ is not due to the low SVFs in FeSe_{1-z}Te_z ($z \geq 0.8$) (23), an Na-NH₃ co-intercalated sample using O₂-annealed FeSe_{0.2}Te_{0.8} was prepared. The magnetic susceptibility measurements indicate that even if the O₂-annealed FeSe_{0.2}Te_{0.8} shows bulk superconductivity (Supplementary Fig. 2a), the superconductivity is still absent for the intercalated sample (Supplementary Fig. 2b). Thus, the absence of superconductivity for the samples with $z \geq 0.8$ should be intrinsic, irrespective of the status of parent compounds.

All samples for both series show Curie-Weiss-like behavior at $H = 1$ kOe. Typical curves are shown in Fig. 3a and Supplementary Fig. 5a. The magnetic behaviors are remarkably different from those of high-temperature-synthesized A_xFe_{2-δ}Ch₂, in which non-Curie-Weiss behaviors, such as positive or weak temperature dependence of $\chi(T)$, are often observed up to room temperature (8, 24). This distinctive behavior should be attributed to the good integrity of the Fe(Se, Te) layers with fewer Fe vacancies in Li/NaNH₃-122. At the high-Te-doping region, there is a magnetic transition appearing below T_p (Fig. 3a and Supplementary Fig. 5a). The bifurcation of ZFC and field-cooling (FC) curves at T_p suggests the presence of a spin-glass (SG) transition. But the detailed measurements indicate that they are different for samples with different Te contents. For (Li/Na)_x(NH₃)_yFe_{2-δ}(Se_{0.1}Te_{0.9})₂, the transitions exhibit strong field dependence (Fig. 3b and Supplementary Fig. 5b). But for Li_x(NH₃)_yFe_{2-δ}Te₂, although the transition shows field dependence at very low fields, possibly due to the small grain size of the sample, the T_p is insensitive to the field when $H \geq 1$ kOe (Fig. 3c). On the other hand, for Li_x(NH₃)_yFe_{2-δ}(Se_{0.1}Te_{0.9})₂, the T_p of the real part of the ac susceptibility $\chi'(T)$ shifts to higher temperature with higher frequency, f (Fig. 3d) and the fitted $K [= \Delta T_p / (T_p \Delta \log f)]$ is 0.0148(9) (Fig. 3f). It is consistent with the values ($0.0045 \leq K \leq 0.08$) found in the canonical SG system, but much smaller than that in a superparamagnet (25). Similar behavior is also observed in Na_x(NH₃)_yFe_{2-δ}(Se_{0.1}Te_{0.9})₂ (Supplementary Fig. 5c and d). In contrast, there is almost no shift

of T_p on $\chi'(T)$ curves with frequency (Fig. 5e and f). These results suggest that the magnetic transitions for Li/NaNH₃-122 ($0.6 \leq z \leq 0.9$) are SG transitions but that Li_x(NH₃)_yFe_{2- δ} Te_z might have an antiferromagnetic transition. The difference could be due to the different Se content. For Li_x(NH₃)_yFe_{2- δ} Te_z, T_p is ~ 30 K at $H = 1$ kOe (Fig. 3c), distinctly different from the antiferromagnetic transition of FeTe with $T_N \sim 60 - 75$ K (9). Thus, the Li-/Na-NH₃ co-intercalation induces new magnetic ordering states at lower temperature by charge-doping and/or changing structural parameters, such as stretching the FeTe plane and increasing the interlayer distance. These magnetic ordering states are more robust than that in FeSe_{1- z} Te _{z} , where the antiferromagnetic state is suppressed significantly when $\sim 10\%$ Se is incorporated into the Te lattice (9).

The phase diagrams of $T_c(z)$ and $T_p(z)$ for Li/NaNH₃-122 are summarized in Fig. 4. There are two T_c s (T_{c1} and T_{c2}) in a two-phase region, similar to FeSe_{1- z} Te _{z} ($0.1 \leq z \leq 0.5$) (Supplementary Fig. 6a), of which the T_c values are determined from $4\pi\chi(T)$ curves (Supplementary Fig. 6b). The T_c s decrease monotonically with Te doping and show similar values for both series at a certain z value, indicating the T_c is not sensitive to the kind of intercalated alkali metals. The suppression of T_c s is similar to that of K_xFe_{2-y}(Se_{1- z} S _{z})₂ (ref. 12), but much milder than that of Rb_{0.8}Fe_{2-y}(Se_{1- z} Te _{z})₂ where doping 15% Te into Se site has already quenched the superconductivity (22). For $z \geq 0.6$, there are magnetic transitions that change from SG transition to an antiferromagnetic one when all of Se is replaced by Te. All samples exhibit paramagnetism at high temperatures. The fact that these phase diagrams of Li/NaNH₃-122 are similar to those of other iron-based SCs, undoubtedly originates from the same key element in these materials, Fe.

On the other hand, the structural analysis indicates that the changes of T_c are intimately related to the structural evolution with Te doping. As shown in Fig. 5a and b, in general, the bond angles of Ch-Fe-Ch (α and β) deviate from the 109.47° of an ideal tetrahedron, and the anion height h that is always larger than 1.38 Å also increases with Te doping for Li/NaNH₃-122 and FeSe_{1- z} Te _{z} . Both trends agree with the empirical relations between structure and T_c mentioned above (11, 12); therefore, the suppression of T_c in Li/NaNH₃-122 could be ascribed to increasing distortion of the

FeCh tetrahedron and moving of anions away from the Fe plane. These parameters are related to each other by the equations: $h = d_{\text{Fe-Pn}} \cos(\alpha/2)$, and $\sin(\beta/2)/\sin(\alpha/2) = [1/2 + (2w-1/2)^2(c/a)^2]^{1/2}$ for Li/NaNH₃-122 ($= [1/2 + 4w^2(c/a)^2]^{1/2}$ for FeSe_{1-z}Te_z), where $d_{\text{Fe-Pn}}$ is the Fe-Pn bond length, w is the c -axial fractional coordination, and c and a are lattice parameters for c and a axes; therefore, it is difficult to distinguish which parameter is dominant in T_c . On the other hand, these empirical relations cannot explain the remarkably low T_c in FeSe_{1-z}Te_z even with similar α/β and h to those of Li/NaNH₃-122 and the higher T_c in FeSe_{1-z}Te_z with Te doping along with the larger distortion of the Fe-Ch tetrahedron and h .

Besides α/β and h , the interlayer distance d between FeCh layers is also considered a key parameter influencing T_c (26, 27). The T_c increases with increasing d and then becomes saturated at ~ 45 K above 9 Å (26, 27). A similar trend is also observed in β -HfNCl. The increase of T_c with d is attributed to the enhancement of Fermi surface (FS) nesting, originating from the reduced dispersion along the c axis, i.e., the less warps of FSs (28, 29). The saturation with slowly decreasing T_c of electron-doped β -HfNCl for $d > 15$ Å might be coupled with a Coulomb interaction between the layers (28). Thus, the weakening effect of d on the warp of FSs will diminish when its value is beyond certain threshold. As shown in Fig. 5c, the d values increase monotonically with increasing Te content for all three series, and the d values of Li/NaNH₃-122 are remarkably larger than those of FeSe_{1-z}Te_z. Because the d values of FeSe_{1-z}Te_z are small, the parameter d may play a more important role in influencing T_c than α/β and h . But for Li/NaNH₃-122, the d values are close to 9 Å and its effect on T_c might become weak. Other factors, such as α/β and h , etc., will dominate T_c .

Although the degree of charge-doping may be not the dominant factor on T_c for Li/NaNH₃-122, it has to be considered as the third parameter influencing T_c of FeCh-based SCs since K_{0.6}(NH₃)_yFe₂Se₂ and K_{0.3}(NH₃)_yFe₂Se₂ show different T_c s at 30 K and 44 K (18). But the degree of charge-doping could not determine the T_c solely because Li-intercalation into FeSe by the electrochemical method does not enhance T_c significantly (30), in contrast to the Li/NH₃ co-intercalation.

Therefore, although the T_c may be controlled by α/β and h for Li/NaNH₃-122, the

superconductivity in FeCh-based SCs should be controlled by more factors, closely related to the electronic structure. They include (1) the interlayer distance that could control the dispersion of FSs along the k_z direction; (2) the bond angles of Ch-Fe-Ch and the anion height that could determine the shape of FSs in the $k_x - k_y$ plane; and (3) the degree of charge-doping that is related to the position of Fermi energy level. This conclusion could explain the trend of T_c s and resolve the apparent contradictions observed in FeCh-based SCs. The highest T_c should result not from optimizing one of these parameters but from an optimal combination, i.e., a larger d with more regular FeCh tetrahedron and better h closer to the optimal value ($\sim 1.44 \text{ \AA}$, not necessarily the same as the optimal one for FePn-based SCs) as well as a close-to-optimal degree of charge-doping. It is different from FePn-based SCs where superconductivity is usually determined by a single parameter (a/β or h). This difference should originate from the distinctively structural features of these two families. For FePn-based SCs, the FePn layers must be negatively charged and thus the blocking layers with positive valence are required. This necessity may limit the effects of the charge-doping level and interlayer distance on T_c . In contrast, for FeCh-based SCs, the neutrality of the FeCh layers relaxes these restrictions and these factors could play important roles in determining the T_c .

In summary, magnetic ordering states were observed in the vicinity of the superconducting state in Li/NaNH₃-122. This universality strongly indicates the intimate relation between superconductivity and magnetism, suggesting the possible existence of an unconventional superconducting mechanism in Li/NaNH₃-122. In contrast to this universality, the factors influencing T_c are not completely the same for both FePn- and FeCh-based SCs. T_c is sensitive to more factors in FeCh-based SCs than in FePn-based ones, possibly because of the distinctly different chemical features of the two families. It suggests that there are several ways to control superconductivity in FeCh-based SCs. These findings will not only shed light on exploring new iron-based SCs, especially FeCh-based SCs, with the higher T_c , but also help us to understand the relationship among structure, electronic structure and superconductivity.

Methods

Synthesis. The highly-pure powder Fe(Se,Te) precursors were synthesized using solid-state reactions. The iron granules (Alfa, 99.98%), selenium grains (Kojundo, 99.99%) and Te grains (Kojundo, 99.999%) were placed into alumina crucibles and sealed in silica ampoules. The samples were heated to 1323 K for 30 h and kept at 1323 K for 24 h, then annealed at 673 K for 50 h, and finally furnace-cooled to room temperature. The obtained Fe(Se,Te) parent compounds were ground into powder and loaded into a Taiatsu Glass TVS-N₂ high-pressure vessel (30 ml) with alkali-metal pieces (Li/Na : Fe(Se,Te) = 1 : 2 molar ratio). A magnetic stirrer was also loaded and the vessel was closed. All of above processes were carried out in an argon-filled glove box with an O₂ and H₂O content below 1 ppm. The vessel was taken out from the glove box and connected to a vacuum/NH₃ gas line equipped with a molecular pump and mass-flow controller. Before introducing NH₃, the vessel was evacuated using a molecular pump ($\sim 5 \times 10^{-2}$ Pa) and placed in a bath of ethanol cooled by liquid nitrogen (~ 223 K). Then, the ammonia cylinder and regulator were then opened and 5 - 10 g of NH₃ was condensed into the vessel. After that, the reaction vessel was closed and stirred for $\sim 3 - 10$ h at 223 - 243 K. When the intercalated process was finished, the vessel was opened and the solutions were evaporated at an ambient pressure. For the Li and NH₃ co-intercalated samples, the vessel was further evacuated to $\sim 10^{-2}$ Pa using a molecular pump for ~ 0.5 h in order to remove the NH₃-rich phase in the samples (19).

Characterization. The powder X-ray diffraction (PXRD) patterns of products were measured by a Bruker diffractometer model D8 ADVANCE with Mo- K_{α} radiations ($\lambda = 0.7107$ Å) at room temperature. The samples were loaded into thin-walled capillary tubes (diameter = 0.5 mm) and then rotated during the measurement in order to eliminate the preferred orientation of samples. The Rietveld refinement of patterns was performed using code TOPAS4 (Bruker AXS). Magnetic susceptibility was measured by a vibrating sample magnetometer (SVSM, Quantum Design). The chemical compositions of the samples were determined by energy-dispersive X-ray

analysis (EDX). The compositions were determined as the average values of 20 points. The contents of nitrogen in the samples were determined using an ion chromatography (IC) technique (31). Typically, 10 mg of the sample was dissolved in 5 mol/L HF aqueous solution, and was diluted by adding water. The resultant solution was analyzed by IC with a Shimadzu CDD-10A conductivity detector.

References

1. Kamihara Y, Watanabe T, Hirano M, Hosono H (2008) Iron-Based Layered Superconductor $\text{La}[\text{O}_{1-x}\text{F}_x]\text{FeAs}$ ($x = 0.05 - 0.12$) with $T_c = 26$ K. *J Am Chem Soc* 130(11): 3296-3297.
2. De la Cruz C, et al. (2008) Magnetic order close to superconductivity in the iron-based layered $\text{LaO}_{1-x}\text{F}_x\text{FeAs}$ systems. *Nature* 453(7197): 899-902.
3. Johnston DC (2010) The puzzle of high temperature superconductivity in layered iron pnictides and chalcogenides. *Adv Phys* 59(6): 803-1061.
4. Mazin II, Singh DJ, Johannes MD, Du MH (2008) Unconventional Superconductivity with a Sign Reversal in the Order Parameter of $\text{LaFeAsO}_{1-x}\text{F}_x$. *Phys Rev Lett* 101(5): 057003.
5. Dong J, et al. (2008) Competing orders and spin-density-wave instability in $\text{LaO}_{1-x}\text{F}_x\text{FeAs}$. *EPL* 83(2): 27006.
6. Hsu FC, et al. (2008) Superconductivity in the PbO-type structure $\alpha\text{-FeSe}$, *Proc Natl Acad Sci USA* 105(38): 14262-14264.
7. Guo JG, et al. (2010) Superconductivity in the iron selenide $\text{K}_x\text{Fe}_2\text{Se}_2$ ($0 \leq x \leq 1.0$). *Phys Rev B* 82(18): 180520(R).
8. Lei HC, et al. (2011) Phase Diagram of $\text{K}_x\text{Fe}_{2-y}\text{Se}_{2-z}\text{S}_z$ and the suppression of its superconducting state by an $\text{Fe}_2\text{-Se/S}$ tetrahedron distortion. *Phys Rev Lett* 107(13): 137002.
9. Liu TJ, et al. (2010) From $(\pi, 0)$ magnetic order to superconductivity with (π, π) magnetic resonance in $\text{Fe}_{1.02}\text{Te}_{1-x}\text{Se}_x$. *Nat Mater* 9(9): 718-720.
10. Chen T-K, et al. (2014) Fe-vacancy order and superconductivity in tetragonal $\beta\text{-Fe}_{1-x}\text{Se}_x$. *Proc Natl Acad Sci USA* 111(1): 63-68.
11. Lee CH, et al. (2012) Relationship between crystal structure and superconductivity in iron-based superconductors. *Solid State Commun* 152(8):

- 644-648.
12. Mizuguchi Y, Takano Y (2010) Review of Fe Chalcogenides as the Simplest Fe-Based Superconductor. *J Phys Soc Jpn* 79(10): 102001.
 13. Margadonna S, et al. (2009) Pressure evolution of the low-temperature crystal structure and bonding of the superconductor FeSe ($T_c = 37$ K). *Phys Rev B* 80(6): 064506.
 14. Medvedev S, et al. (2009) Electronic and magnetic phase diagram of β -Fe_{1.01}Se with superconductivity at 36.7 K under pressure. *Nat Mater* 8(8): 630-633.
 15. Lu XF, et al. (2013) Superconductivity in LiFeO₂Fe₂Se₂ with anti-PbO-type spacer layers. *Phys Rev B* 89(2): 020507(R).
 16. Ying TP, et al. (2012) Observation of superconductivity at 30 ~ 46 K in A_xFe₂Se₂ (A = Li, Na, Ba, Sr, Ca, Yb, and Eu). *Sci Rep* 2: 426.
 17. Burrard-Lucas M, et al. (2013) Enhancement of the superconducting transition temperature of FeSe by intercalation of a molecular spacer layer. *Nat Mater* 12(1): 15-19.
 18. Ying TP, et al. (2013) Superconducting Phases in Potassium-Intercalated Iron Selenides. *J. Am. Chem. Soc.* 135(8): 2951-2954.
 19. Sedlmaier SJ, et al. (2014) Ammonia-rich high-temperature superconducting intercalates of iron selenide revealed through time-resolved in situ x-ray and neutron diffraction. *J Am Chem Soc* 136(2): 630-633.
 20. Wang Z, et al. (2011) Microstructure and ordering of iron vacancies in the superconductor system K_yFe_xSe₂ as seen via transmission electron microscopy. *Phys Rev B* 83(14): 140505(R).
 21. Chen F, et al. (2011) Electronic Identification of the Parental Phases and Mesoscopic Phase Separation of K_xFe_{2-y}Se₂ Superconductors. *Phys Rev X* 1(2): 021020.
 22. Gu D, et al. (2012) Correlation between superconductivity and antiferromagnetism in Rb_{0.8}Fe_{2-y}Se_{2-x}Te_x single crystals. *Phys Rev B* 85(17): 174523.
 23. Kawasaki Y, et al. (2012) Phase diagram and oxygen annealing effect of FeTe_{1-x}Se_x iron-based superconductor. *Solid State Commun* 152(13): 1135-1138.
 24. Liu RH, et al. (2011) Coexistence of superconductivity and antiferromagnetism in

- single crystals $A_{0.8}Fe_{2-y}Se_2$ ($A = K, Rb, Cs, Tl/K$ and Tl/Rb): Evidence from magnetization and resistivity. *EPL* 94(2): 27008.
25. Mydosh JA (1993) Spin Glasses: An Experimental Introduction (Taylor & Francis, London).
 26. Zheng L, et al. (2013) Superconductivity in $(NH_3)_yCs_{0.4}FeSe$. *Phys Rev B* 88(9): 094521.
 27. Noji T, Hatakeda T, Hosono S, Kawamata T, Kato M, Koike Y (2014) Synthesis and post-annealing effects of alkaline-metal-ethylenediamine-intercalated superconductors $A_x(C_2H_8N_2)_yFe_{2-z}Se_2$ ($A = Li, Na$) with $T_c = 45$ K. *Physica C* Article in Press.
 28. Zhang S, Tanaka M, Zhu H, Yamanaka S (2013) Superconductivity of layered β -HfNCl with varying electron-doping concentrations and interlayer spacings. *Supercond Sci Technol* 26(8): 085015.
 29. Takano T, Kishiume T, Taguchi Y, Iwasa Y (2008) Interlayer-Spacing Dependence of T_c in Li_xM_yHfNCl (M: Molecule) Superconductors. *Phys Rev Lett* 100(24): 247005.
 30. Abe H, Noji T, Kato M, Koike Y (2009) Electrochemical Li-intercalation into the Fe-based superconductor $FeSe_{1-x}Te_x$. *Physica C* 470(S1): S487-S488.
 31. Hayashi F, Ishizu K-I, Iwamoto M (2010) Fast and Almost Complete Nitridation of Mesoporous Silica MCM-41 with Ammonia in a Plug-Flow Reactor. *J Am Ceram Soc* 93(1): 104-110.

Acknowledgements

This work was supported by the Funding Program for World-Leading Innovative R&D on Science and Technology (FIRST) and MEXT Element Strategy Initiative to form a core research center, Japan.

Author contributions

[†]These authors contributed equally to this work.

H. H. provided strategy and advice for the material exploration. H. L. and J. G. performed the sample fabrication, measurements and fundamental data analysis. F. H. set up the apparatus for low-temperature ammonothermal experiments and analyzed

the chemical composition of products using the IC technique. H. L. and H. H. wrote the manuscript based on discussion with all the authors.

*To whom correspondence may be addressed. E-mail: hosono@msl.titech.ac.jp

Additional information

This article contains supporting information.

The authors declare no conflict of interest.

Figure captions

Figure 1. Structural evolution of $(\text{Li/Na})_x(\text{NH}_3)_y\text{Fe}_{2-\delta}(\text{Se}_{1-z}\text{Te}_z)_2$. The fitted (a) c -axial and (b) a -axial lattice parameters for $(\text{Li/Na})_x(\text{NH}_3)_y\text{Fe}_{2-\delta}(\text{Se}_{1-z}\text{Te}_z)_2$ and $\text{FeSe}_{1-z}\text{Te}_z$. All the error bars are statistical errors from the TOPAS refinement. (b) The crystal structure of $(\text{Li/Na})_x\text{N}_y\text{Fe}_{2-\delta}(\text{Se}_{1-z}\text{Te}_z)_2$. Because the position of H atoms cannot be determined due to the smaller scattering factor of hydrogen, the H atoms are not plotted in the crystal structure. (b) The PXRD pattern of $\text{Li}_x(\text{NH}_3)_y\text{Fe}_{2-\delta}\text{Te}_2$.

Figure 2. Low-field magnetic properties of $(\text{Li/Na})_x(\text{NH}_3)_y\text{Fe}_{2-\delta}(\text{Se}_{1-z}\text{Te}_z)_2$. Temperature dependences of magnetic susceptibility $4\pi\chi(T)$ for (a) $\text{Li}_x(\text{NH}_3)_y\text{Fe}_{2-\delta}(\text{Se}_{1-z}\text{Te}_z)_2$ and (b) $\text{Na}_x(\text{NH}_3)_y\text{Fe}_{2-\delta}(\text{Se}_{1-z}\text{Te}_z)_2$ at low-temperature region with $H = 10$ Oe. For clarity, only the zero-field-cooling (ZFC) curves are shown.

Figure 3. High-field dc and low-field ac magnetizations of $(\text{Li/Na})_x(\text{NH}_3)_y\text{Fe}_{2-\delta}(\text{Se}_{1-z}\text{Te}_z)_2$. (a) $\chi(T)$ curves of $\text{Li}_x(\text{NH}_3)_y\text{Fe}_{2-\delta}(\text{Se}_{1-z}\text{Te}_z)_2$ ($z = 0.4, 0.7$ and 0.8) at $H = 1$ kOe with ZFC and field-cooling (FC) modes. (b) and (c) Temperature dependence of magnetic moment $M(T)$ at various fields for $\text{Li}_x(\text{NH}_3)_y\text{Fe}_{2-\delta}(\text{Se}_{1-z}\text{Te}_z)_2$ with $z = 0.9$ and $z = 1.0$, respectively. For $\text{Li}_x(\text{NH}_3)_y\text{Fe}_{2-\delta}\text{Te}_2$, the kinks at $T \sim 68$ K with $H \geq 10$ kOe are due to the minor second phase of FeTe. (d)

and (e) The real part of ac susceptibility $\chi'(T)$ at $H_{ac} = 1$ Oe with various frequencies f for $\text{Li}_x(\text{NH}_3)_y\text{Fe}_{2-\delta}(\text{Se}_{1-z}\text{Te}_z)_2$ with $z = 0.9$ and $z = 0.1$, respectively. The arrows show the T_p s on $\chi'(T)$ curves. (f) Frequency dependence of peak positions T_p s for $\text{Li}_x(\text{NH}_3)_y\text{Fe}_{2-\delta}(\text{Se}_{1-z}\text{Te}_z)_2$ with $z = 0.9$ and $z = 1.0$. The red solid line is the result of a linear fit.

Figure 4. Superconducting and magnetic phase diagrams of $(\text{Li}/\text{Na})_x(\text{NH}_3)_y\text{Fe}_{2-\delta}(\text{Se}_{1-z}\text{Te}_z)_2$. The T_p s are determined from $\chi(T)$ curves at $H = 1$ kOe. The red solid and empty squares represent two superconducting transition temperatures T_{c1} and T_{c2} of $\text{Li}_x(\text{NH}_3)_y\text{Fe}_{2-\delta}(\text{Se}_{1-z}\text{Te}_z)_2$. The blue solid and empty circles represent T_{c1} and T_{c2} of $\text{Na}_x(\text{NH}_3)_y\text{Fe}_{2-\delta}(\text{Se}_{1-z}\text{Te}_z)_2$. The green solid squares/violet solid circles represent the spin glass transition temperatures T_p of $(\text{Li}/\text{Na})_x(\text{NH}_3)_y\text{Fe}_{2-\delta}(\text{Se}_{1-z}\text{Te}_z)_2$. The green empty square represents the antiferromagnetic transition temperature T_p of $\text{Li}_x(\text{NH}_3)_y\text{Fe}_{2-\delta}\text{Te}_2$. PM, paramagnetism; SC-Phase 1, superconductivity of Phase 1; SC-Phase 2, superconductivity of Phase 2; SG, spin glass; AFM, antiferromagnetism.

Figure 5. Comparative structure analysis of $(\text{Li}/\text{Na})_x(\text{NH}_3)_y\text{Fe}_{2-\delta}(\text{Se}_{1-z}\text{Te}_z)_2$ and $\text{FeSe}_{1-z}\text{Te}_z$. (a) Ch-Fe-Ch bond angles α and β , (b) anion height h , and (c) interlayer distance d between Fe-Ch layers of $(\text{Li}/\text{Na})_x(\text{NH}_3)_y\text{Fe}_{2-\delta}(\text{Se}_{1-z}\text{Te}_z)_2$ and $\text{FeSe}_{1-z}\text{Te}_z$ as a function of z . Insets of (a), (b) and (c) show the definitions of these parameters in the structure. The dotted pink line in (a) shows the bond angle of a regular FeCh tetrahedron.

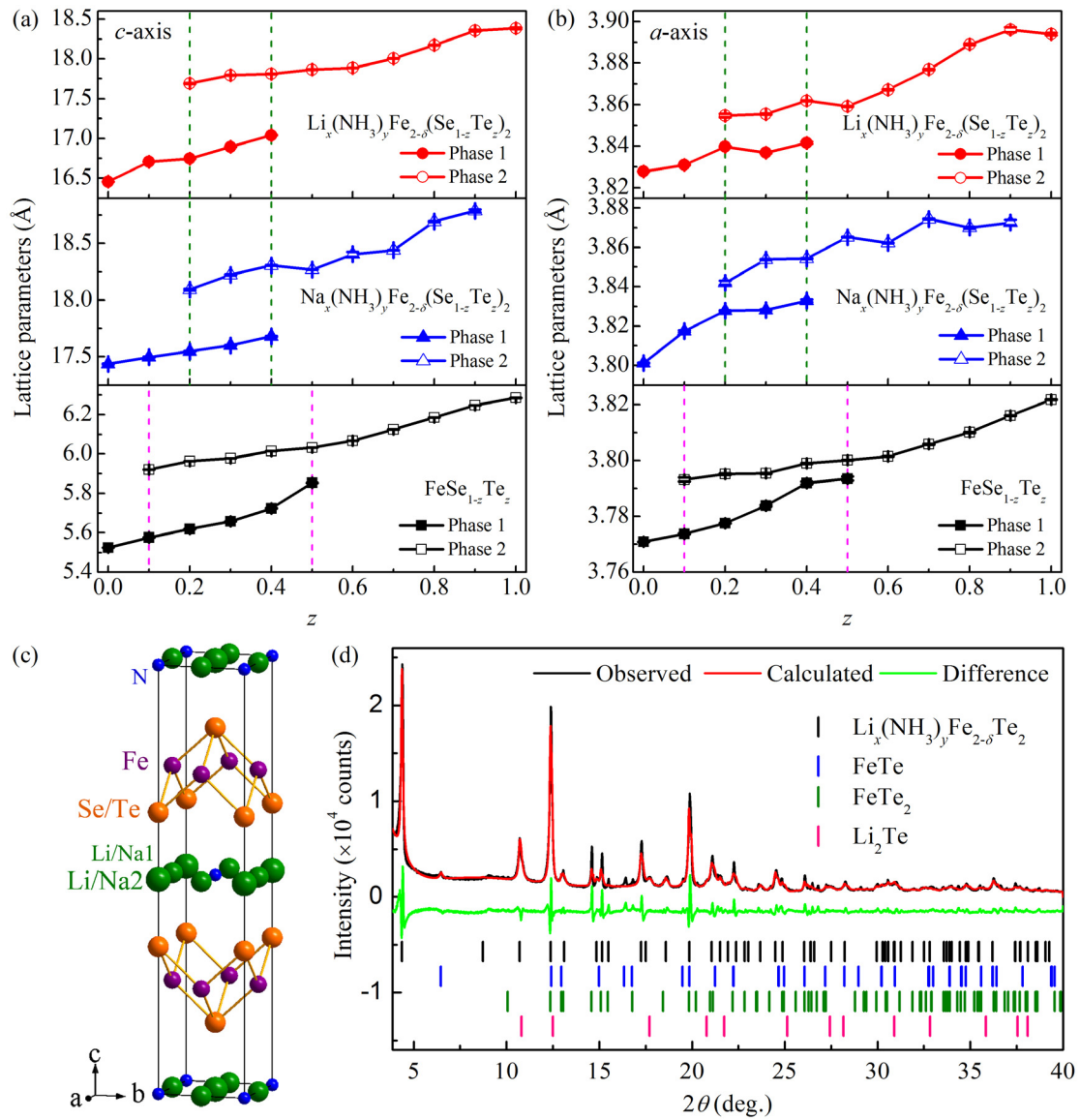


Fig.1 Lei et al.

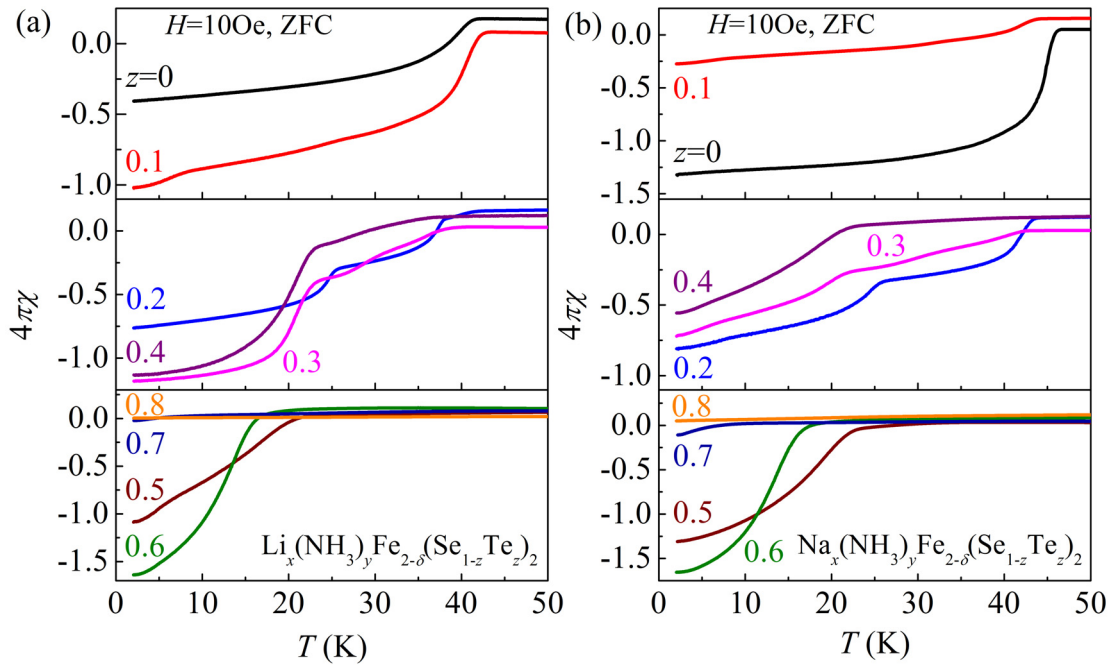


Fig. 2 Lei et al.

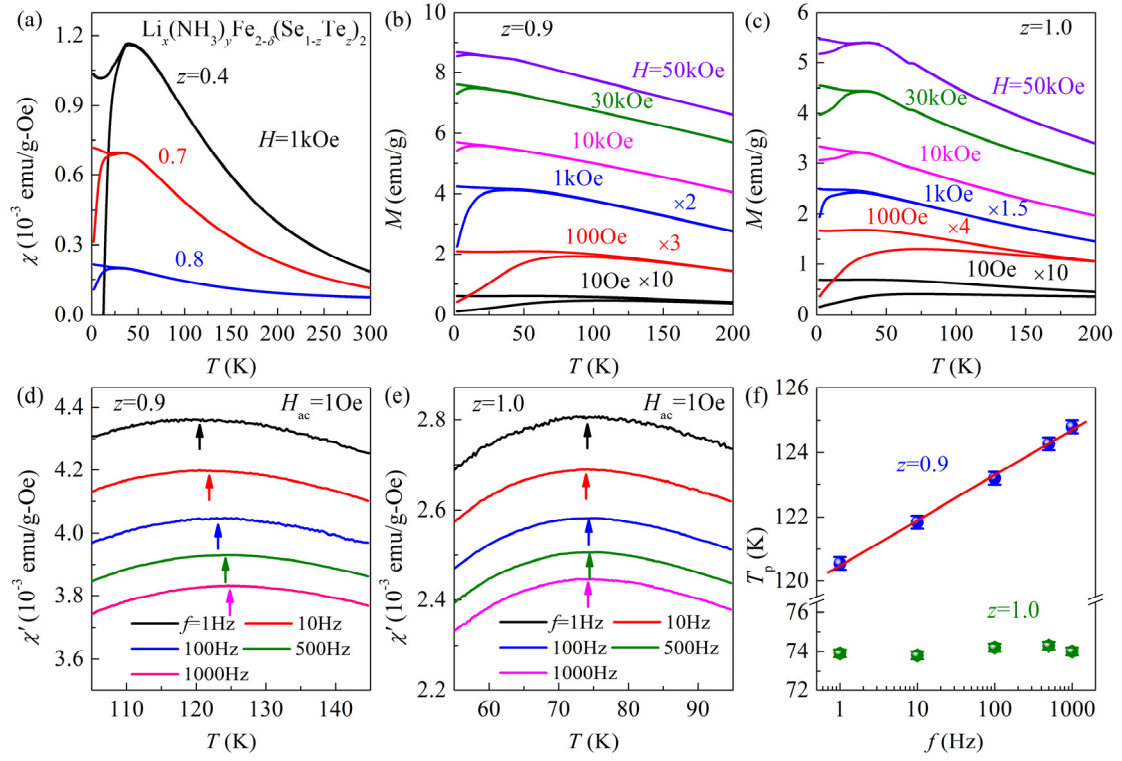


Fig. 3 Lei et al.

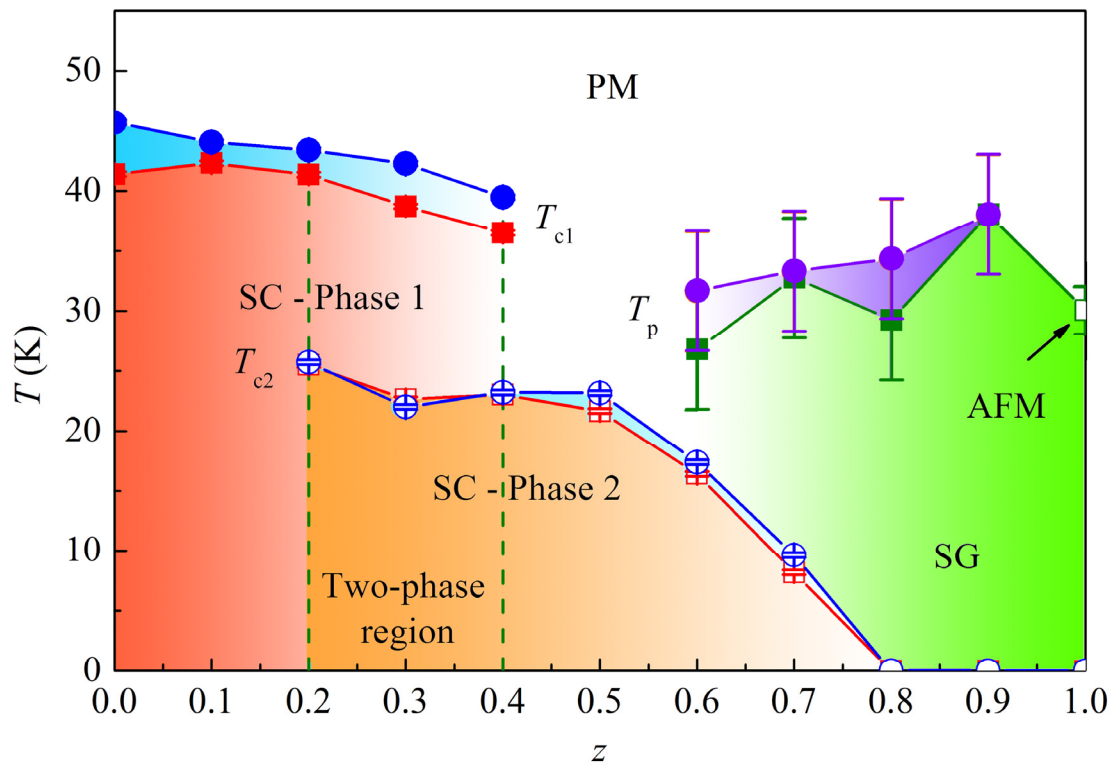


Fig. 4 Lei et al.

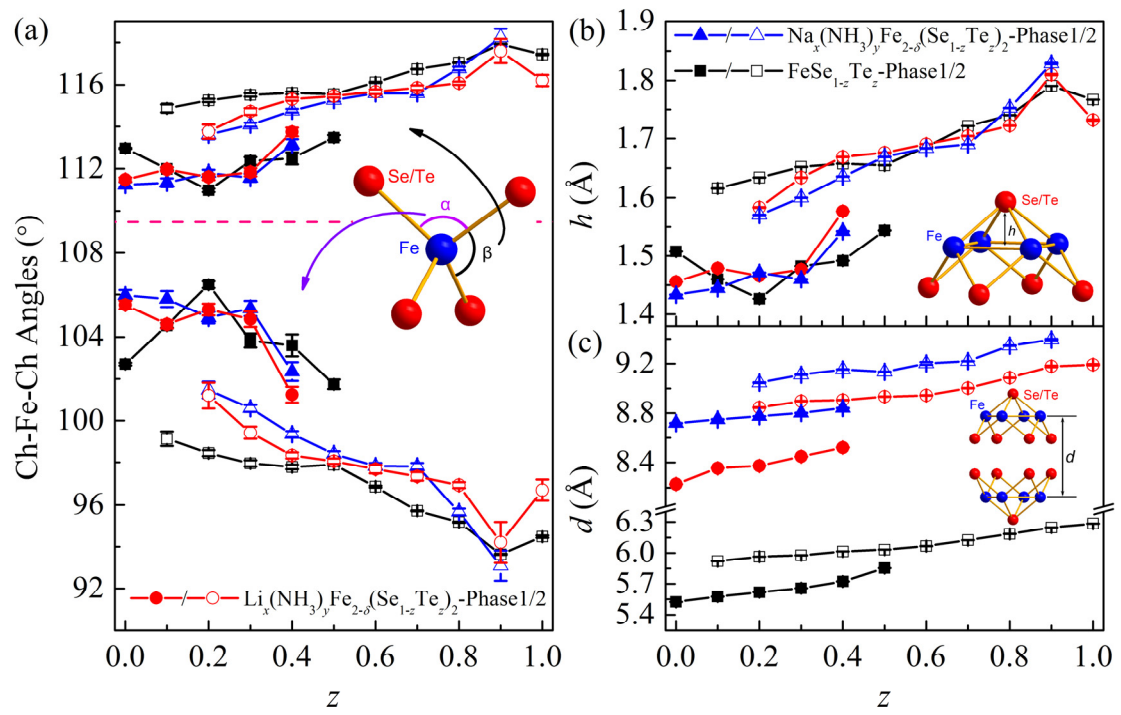


Fig. 5 Lei et al.

**Controlling factors of superconductivity and emergence of
magnetism in $A_x(\text{NH}_3)_y\text{Fe}_{2-\delta}(\text{Se}_{1-z}\text{Te}_z)_2$ (A = Li and Na)**

Hechang Lei,^{1,†} Jiangang Guo,^{1,†} Fumitaka Hayashi,² and Hideo Hosono,^{1,2,3,}*

¹ Materials Research Center for Element Strategy, Tokyo Institute of
Technology, Yokohama 226-8503, Japan

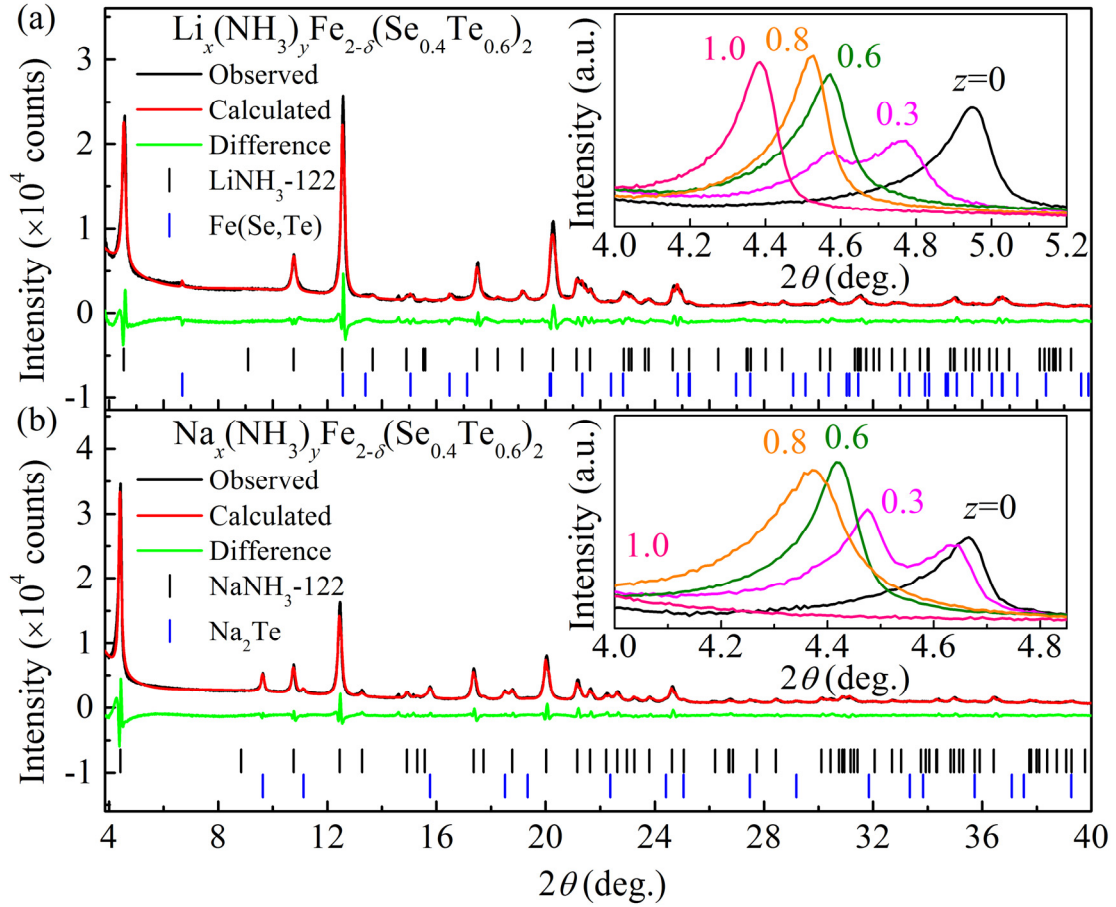
² Frontier Research Center, Tokyo Institute of Technology, Yokohama 226-8503,
Japan

³ Materials and Structures Laboratory, Tokyo Institute of Technology,
Yokohama 226-8503, Japan

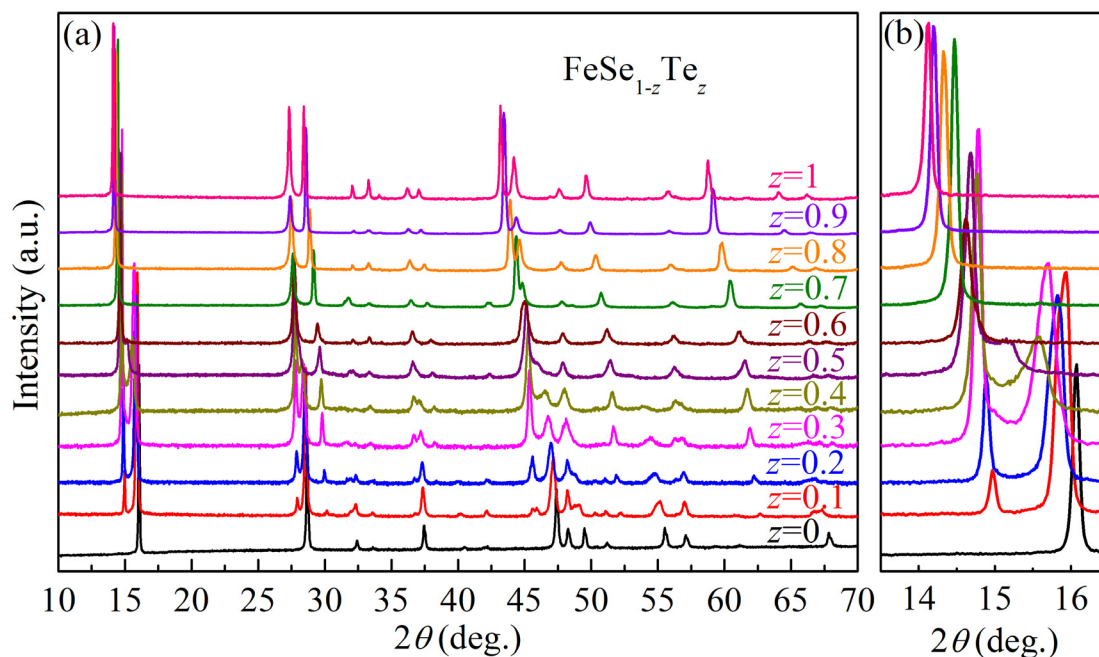
Supporting Information

[†]These authors contributed equally to this work.

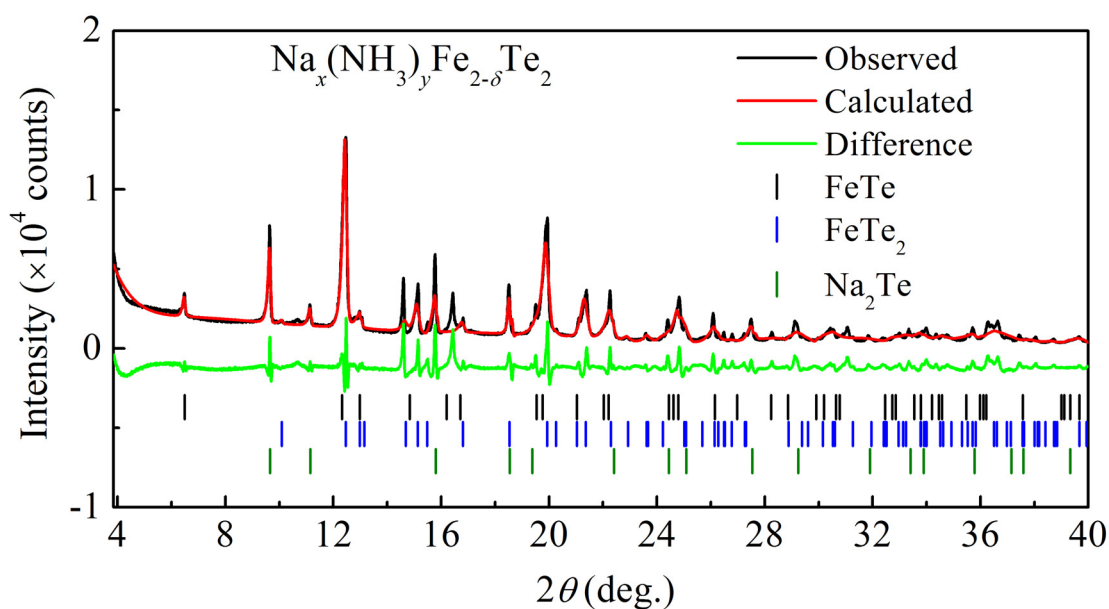
*Corresponding author: hosono@mssl.titech.ac.jp



Supplementary Fig. 1: Structural evolution of $(\text{Li}/\text{Na})_x(\text{NH}_3)_y\text{Fe}_{2-\delta}(\text{Se}_{1-z}\text{Te}_z)_2$. PXRd patterns and fitted results of (a) $\text{Li}_x(\text{NH}_3)_y\text{Fe}_{2-\delta}(\text{Se}_{0.4}\text{Te}_{0.6})_2$ and (b) $\text{Na}_x(\text{NH}_3)_y\text{Fe}_{2-\delta}(\text{Se}_{0.4}\text{Te}_{0.6})_2$. Other samples with various z values exhibit similar PXRd patterns except for $\text{Na}_x(\text{NH}_3)_y\text{Fe}_{2-\delta}\text{Te}_2$. The structure of $\text{Li}_{0.6}(\text{ND}_{2.8})\text{Fe}_2\text{Se}_2$ is used as an initial model and the structural parameters are obtained from Rietveld refinement. There are trace amounts of second phases like $(\text{Li}/\text{Na})_2\text{Te}$, $\text{Fe}(\text{Se}, \text{Te})_2$ and unreacted $\text{Fe}(\text{Se}, \text{Te})$ existing in the intercalated samples. Insets: enlarged parts of PXRd patterns for (002) diffractions for $(\text{Li}/\text{Na})_x(\text{NH}_3)_y\text{Fe}_{2-\delta}(\text{Se}_{1-z}\text{Te}_z)_2$ with $z = 0, 0.3, 0.6, 0.8$, and 1.0 .



Supplementary Fig. 2: Structural evolution of $\text{FeSe}_{1-z}\text{Te}_z$. (a) PXRD patterns of $\text{FeSe}_{1-z}\text{Te}_z$. (b) Enlarged part of XRD patterns showing the (001) peak.



Supplementary Fig. 3: PXRD patterns of reaction products after immersing FeTe into Na-NH_3 solution. Only binary phases such as FeTe , FeTe_2 and Na_2Te appear.

Supplementary Table 1: Nominal and actual average compositions of two series of

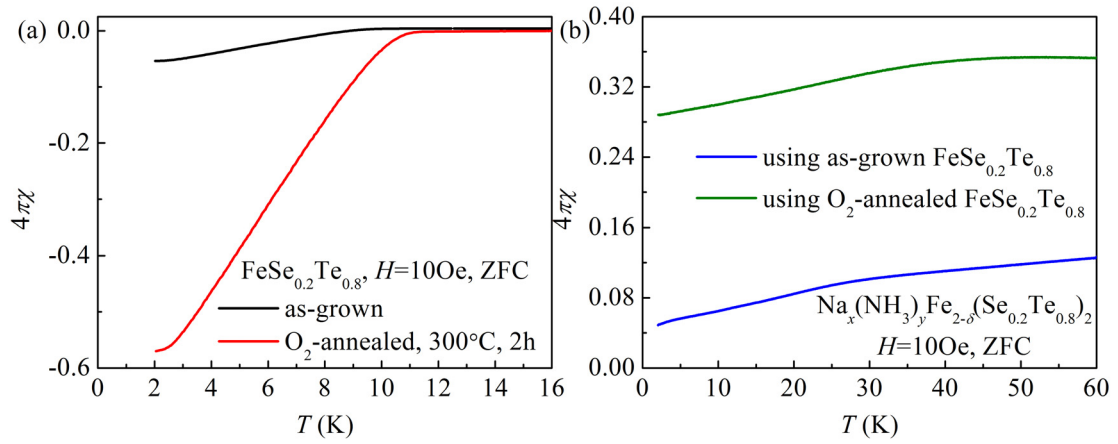
(Li/Na)_x(NH₃)_yFe_{2-δ}(Se_{1-z}Te_z)₂ measured by energy-dispersive X-ray analysis (EDX) method.*

| Nominal <i>z</i> | Li _x (NH ₃) _y Fe _{2-δ} (Se _{1-z} Te _z) ₂ | | Na _x (NH ₃) _y Fe _{2-δ} (Se _{1-z} Te _z) ₂ | | |
|------------------|---|-------------------------|---|-------------------------|-------------------------|
| | Actual average δ | Actual average <i>z</i> | Actual average <i>x</i> | Actual average δ | Actual average <i>z</i> |
| 0.0 | 0.18(17) | 0.00 | 0.74(16) | 0.22(20) | 0.00 |
| 0.1 | 0.10(18) | 0.07(2) | 0.46(11) | 0.06(16) | 0.07(5) |
| 0.2 | 0.09(15) | 0.17(4) | 0.67(12) | 0.08(11) | 0.22(7) |
| 0.3 | 0.03(15) | 0.31(2) | 0.44(10) | 0.08(10) | 0.34(14) |
| 0.4 | 0.15(11) | 0.42(8) | 0.67(21) | 0.15(16) | 0.46(4) |
| 0.5 | 0.04(13) | 0.53(4) | 0.83(15) | 0.09(9) | 0.54(2) |
| 0.6 | 0.12(11) | 0.61(2) | 0.67(16) | 0.17(9) | 0.59(3) |
| 0.7 | 0.10(7) | 0.69(1) | 0.70(13) | 0.03(10) | 0.72(1) |
| 0.8 | 0.09(13) | 0.80(2) | 0.54(11) | 0.06(7) | 0.82(3) |
| 0.9 | 0.09(06) | 0.91(2) | 0.59(10) | 0.02(6) | 0.91(2) |
| 1.0 | 0.08(05) | 1.00 | - | - | - |

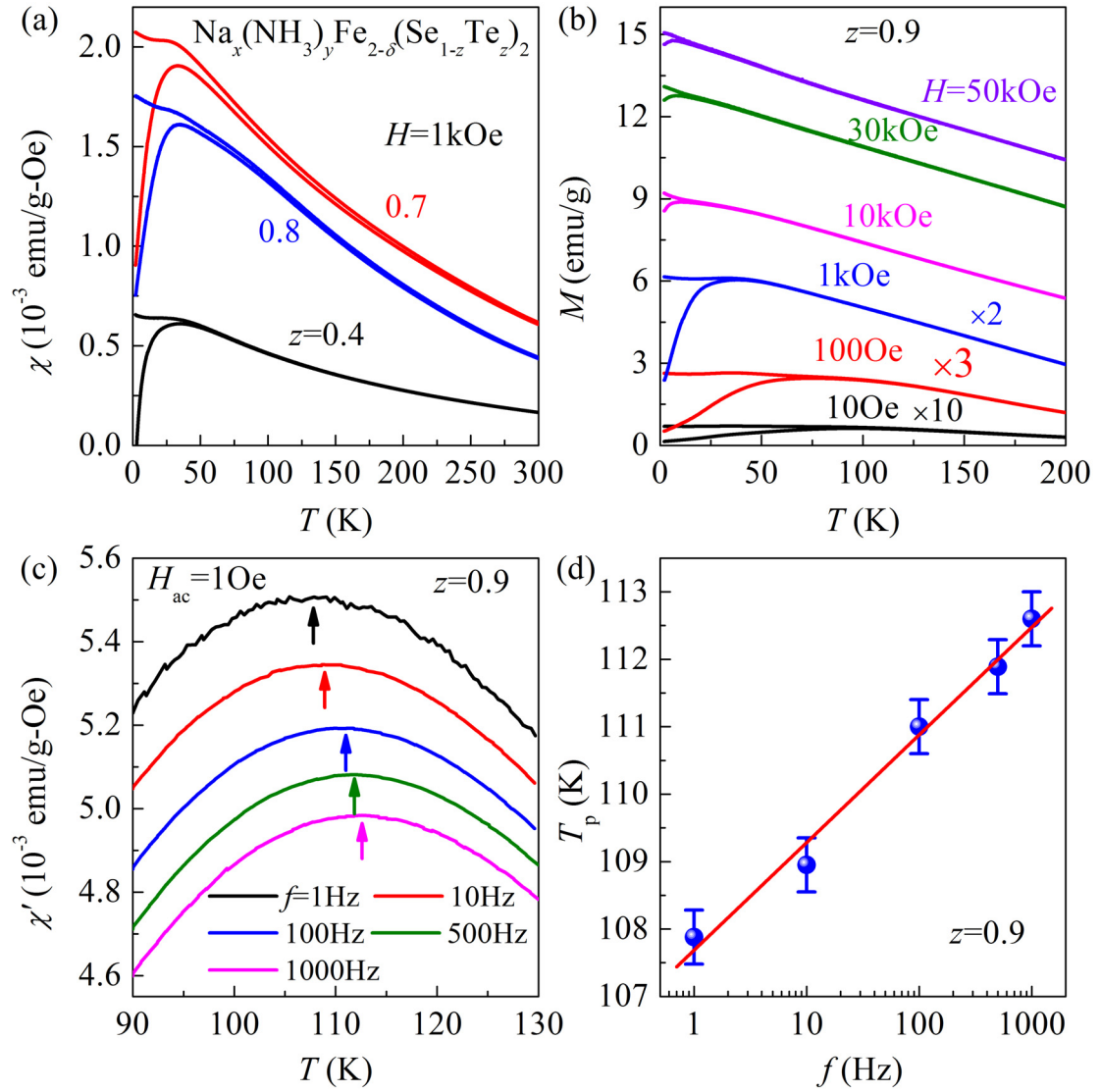
*The Li content in the intercalates cannot be determined by the EDX.

Supplementary Table 2: Nominal and actual average *z* values in FeSe_{1-z}Te_z measured by EDX method

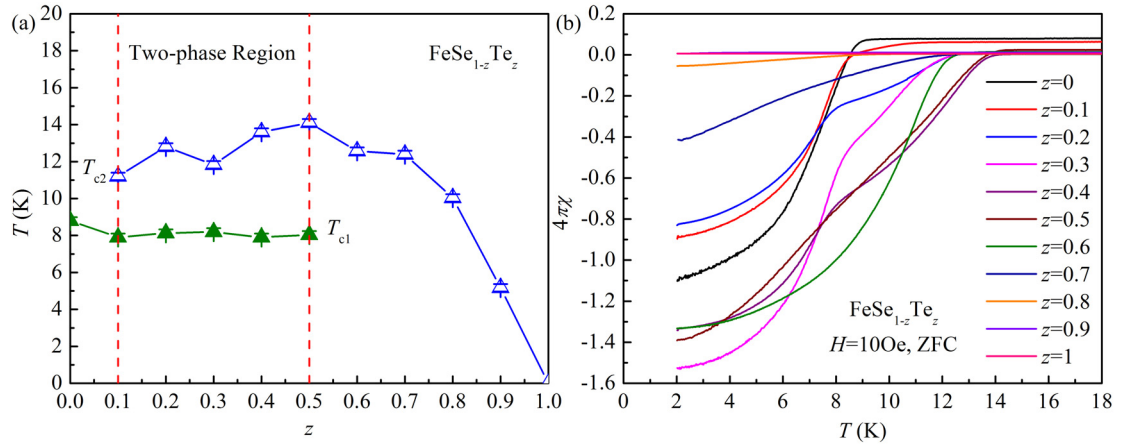
| Nominal <i>z</i> | Actual average <i>z</i> |
|------------------|-------------------------|
| 0.0 | 0.00 |
| 0.1 | 0.08(2) |
| 0.2 | 0.19(4) |
| 0.3 | 0.30(4) |
| 0.4 | 0.38(6) |
| 0.5 | 0.52(4) |
| 0.6 | 0.58(2) |
| 0.7 | 0.71(2) |
| 0.8 | 0.81(2) |
| 0.9 | 0.91(1) |
| 1.0 | 1.00 |



Supplementary Fig. 4: O₂-annealing effects on magnetic properties of $\text{FeSe}_{0.2}\text{Te}_{0.8}$ and $\text{Na}_x(\text{NH}_3)_y\text{Fe}_{2-\delta}(\text{Se}_{0.2}\text{Te}_{0.8})_2$. (a) Magnetic susceptibilities $4\pi\chi(T)$ of as-grown and O₂-annealed $\text{FeSe}_{0.2}\text{Te}_{0.8}$ and (b) $4\pi\chi(T)$ curves of $\text{Na}_x(\text{NH}_3)_y\text{Fe}_{2-\delta}(\text{Se}_{0.2}\text{Te}_{0.8})_2$ prepared using as-grown and O₂-annealed $\text{FeSe}_{0.2}\text{Te}_{0.8}$ at $H = 10$ Oe with zero-field-cooling (ZFC) mode.



Supplementary Fig. 5: Magnetic properties of $\text{Na}_x(\text{NH}_3)_y\text{Fe}_{2-\delta}(\text{Se}_{0.1}\text{Te}_{0.9})_2$. (a) Temperature dependence of the magnetic moment $M(T)$ at various fields. (b) The real part of ac susceptibility $\chi'(T)$ at $H_{ac} = 1 \text{ Oe}$ with various frequencies, f . The arrows show the peak positions, T_p s, on the $\chi'(T)$ curves. (c) Frequency dependence of T_p . The solid line is the result of linear fit. The obtained K ($= \Delta T_p / (T_p \Delta \log f)$) is $0.0117(3)$.



Supplementary Fig. 6: Evolution of physical properties for $\text{FeSe}_{1-z}\text{Te}_z$. (a)

Superconducting phase diagram of $\text{FeSe}_{1-z}\text{Te}_z$ determined from magnetic susceptibility measurements. The green solid and blue empty triangles represent two superconducting transition temperatures T_{c1} and T_{c2} of $\text{FeSe}_{1-z}\text{Te}_z$. (b) $4\pi\chi(T)$ curves of $\text{FeSe}_{1-z}\text{Te}_z$ measured at low-temperature range at $H = 10$ Oe. For clarity, only the ZFC curves are shown.